

# Properties of Near Field Focusing for Cylindrical Dipole Arrays in Enclosed Array Volume

Jiawang Li

**Abstract**—Motivated by large intelligent surface applications, the electric field properties of near field focusing using phase conjugation method are analyzed for cylindrical dipole arrays. Firstly, for the transmitting antennas featuring vertical polarization, the polarization characteristic is decomposed along the  $x$ ,  $y$ , and  $z$  directions. Three typical cases are studied when the focal points are at  $(x_f, 0, 0)$ ,  $(0, y_f, 0)$ , and  $(0, 0, z_f)$ . When the length of the cylindrical dipole array is significantly larger compared to its radius, certain unique insights emerge. When the focal point is positioned along  $(0, 0, z_f)$ , apart from the region on both sides, the ratio between  $E_z$  and  $E_x/E_y$  remains  $\pi/2$ . Additionally, When the focal point is located within the cylinder, the electric field of each polarization is approximately the same everywhere. In other words, beam focusing does not incur losses due to different positions. The focusing resolution of  $E_z$  is the same in the transverse and longitudinal directions. Different from the situation where the 3 - dB focal beam depth is much smaller than the focal beam width for the most of arrays, the resolution in the longitudinal can be improved, respectively. Through a comprehensive grasp of these design principles, we can gain a deeper understanding of the specific areas with significant potential for practical applications.

**Index Terms**—Beam resolution, cylindrical array, wave polarization, beamforming.

## I. INTRODUCTION

**L**ARGE intelligent surface (LIS) [1] is a promising concept for fulfilling tough 6G requirements in sub-10 GHz bands, given the limited frequency spectrum resource. As depicted in Fig. 1, LISs are distributed along the interior walls, and each of them comprises hundreds or even thousands of antenna elements. These elements generate beams that enable indoor wireless communication or power transfer. For instance, they can support communication for mobile phones and Wi-Fi networks while simultaneously charging devices such as smartwatches, ensuring their normal operation.

In this scenario, the electromagnetic waves generated by the LIS through beamforming are no longer far-field plane waves [2] but should instead be regarded as near-field spherical waves [3]-[5]. Consequently, traditional beamforming methods [6]-[7] designed for the far field are no longer applicable, prompting a growing focus on research tailored to the near-field region [8]-[16]. These beamforming methods can be broadly categorized into two types. The first type is

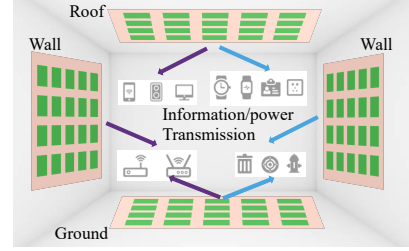


Fig. 1. LIS application scenarios indoors.

based on the conjugate-phase method [8]-[12], while the other is based on various optimization algorithms [13]-[16]. References [8]-[12] conducted research on the beamforming of planar rectangular arrays, planar circular arrays, and arc-shaped linear arrays, with a focus on analyzing their focal point and gain characteristics. However, these studies mainly concentrated on one or two-dimensional antenna arrays and did not take into account the impact of antenna polarization. In references [12]-[16], the authors employed methods such as convex optimization, compressive sensing, and norm regularization to achieve low-sidelobe generation at the focal point. Nevertheless, the synthesis time increased dramatically, reaching even hundreds of seconds [16], which does not allow for real-time focusing. Furthermore, previous work on near-field focusing does not consider the LIS scenario where the array elements are distributed around the focusing point, as in Fig. 1.

Therefore, to address the research gap, this paper conducts an analysis of focusing properties for LIS deployment along a corridor environment, which is modeled using the simplified model of a cylindrical dipole array. Importantly, the effect of polarization is included. The main findings include:

- 1) The intensities of the focal points generated by the electric fields of different polarizations are stable inside the cylinder. This is in contrast to typical planar arrays [8]-[11], where the gain loss occurs when the focal point deviates from the central axis.
- 2) When focal points moves along the  $z$ -axis on the array's axis, the gain of  $E_x$ ,  $E_y$ , and  $E_z$  approaches the normalized constants 8, 8, and  $4\pi$ , respectively, across the entire circular region, except for narrow areas at the edges where the gain is halved.
- 3) For the ratio  $E_x/E_y$ , the peak power of focusing does not occur inside the circle but at a certain position outside the cylinder.
- 4) The electric field  $E_z$  along the length direction of the

Manuscript received xxxx.xx.xx. (Corresponding author: Jiawang Li).

Jiawang Li is with the Department of Electrical and Information Technology, Lund University, 22100 Lund, Sweden (e-mail: jiawang.li@eit.lth.se).

Color versions of one or more of the figures in this letter are available online at <http://ieeexplore.ieee.org>.

Digital Object Identifier 10.1109/AWPL.2025.xxx.

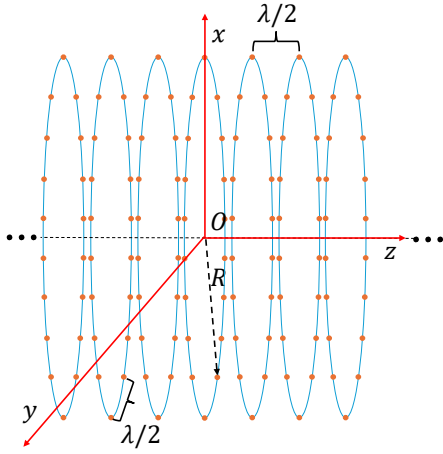


Fig. 2. LIS application scenarios indoors for a long corridor.

array generates a focal point inside the cylinder with nearly the same transverse and longitudinal resolutions.

## II. ARRAY CONFIGURATION AND ANALYSIS

As shown in Fig. 1, the structure consists of multiple circular arrays with their centers aligned along the  $z$ -axis. Each circular array has a radius of  $R$ , and the spacing between antennas on each ring is half a wavelength  $d = \lambda/2$ . Similarly, the spacing between adjacent rings is also  $\lambda/2$ . The circular arrays extend symmetrically along both sides of the  $xy$ -plane. Each antenna element is a vertically polarized dipole and the polarization is along the  $z$ -axis. In this analysis, we neglect coupling between antennas and spatial scattering, considering only the line-of-sight (LOS) channel. All the simulated frequency is under the 6 GHz ( $\lambda = 0.05\text{m}$ ) and radius of the circle is  $20\lambda$  ( $R = 20\lambda$ ).

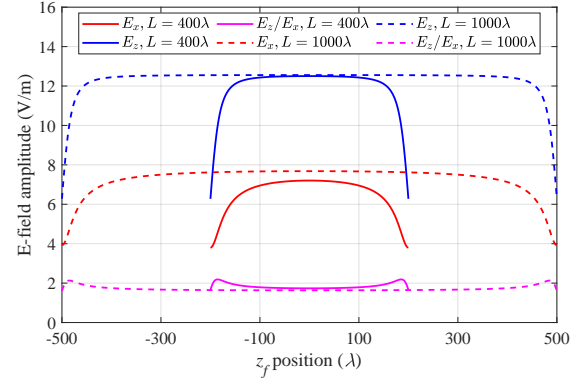
### A. Field Intensity Distribution

Firstly, the focal point is set to  $\mathbf{r}_0 = (x, y, z)$ ,  $z$  is the direction along the corridor length. The position of each element is  $R_n = (R \cos \theta_n, R \sin \theta_n, (m-1)d)$ ,  $\theta_n = \frac{2\pi n}{N}$ , here  $n$  is the index of each element in a circular array, and  $m$  is the number of the circular arrays.  $N$  is the total number of elements in each circular array.  $R$  is the radius of the circular array. Because the polarization direction is parallel to the  $z$ -axis, the polarization vector is  $\hat{\mathbf{p}} = (0, 0, 1)$ . Based on [9], the expressions for the electric field components along the three directions can be derived as follows

$$E_x = \sum_{m=-M/2}^{M/2} \sum_{n=1}^N [d \cdot (m-1) - z] (x - R \cos \theta_n) Q(x, y, z), \quad (1)$$

$$E_y = \sum_{m=-M/2}^{M/2} \sum_{n=1}^N [d \cdot (m-1) - z] (y - R \sin \theta_n) Q(x, y, z), \quad (2)$$

$$E_z = \sum_{m=-M/2}^{M/2} \sum_{n=1}^N P(x, y) Q(x, y, z). \quad (3)$$

Fig. 3. The electric field amplitudes for  $E_x$  and  $E_z$  along the  $(0, 0, z)$ .

here,  $Q(x, y, z)$  represents a common factor shared by the three formulas, which includes both the amplitude term and the phase term. Their expressions are given as:

$$Q(x, y, z) = \frac{E_0 e^{-jk\sqrt{P(x,y)+(d_m-z)^2}}}{[P(x, y) + (d_m - z)^2]^{3/2}}, \quad (4)$$

$$P(x, y) = (x - R \cos \theta_n)^2 + (y - R \sin \theta_n)^2, \quad (5)$$

where  $E_0 = j\eta I_0 L k / (4\pi)$ ,  $I_0$  and  $L$  are the current and the length of the dipole, and  $\varepsilon_0$  is the dielectric constant in a vacuum and  $E_0 = 1$  V/m. The expression of the electric field components reveals that each component contains a distinct and unique part. This indicates the anisotropic nature of the electric field across the  $x$ ,  $y$ , and  $z$  directions. When the number of elements is sufficiently large, each circular ring can be approximated as a continuous integral over the range  $[0, 2\pi]$ . Similarly, for the longitudinal dimension along the  $z$ -axis, if the length is sufficiently long, it can be treated as a continuous integral over the range  $[-L/2, L/2]$ .

By applying the conjugate-phase method to compensate for the phase terms in the electric field, the following formula can be obtained

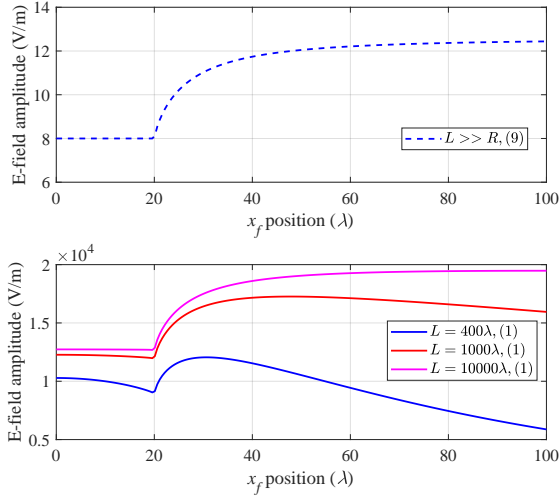
$$E_x(z_f) = \int_{-L/2}^{L/2} \int_0^{2\pi} \frac{|l - z_f| |x - R \cos \theta|}{[P(x, y) + (l - z_f)^2]^{3/2}} d\theta dl. \quad (6)$$

As a result, the theoretically obtainable closed-form is [17]

$$E_x(z_f) = 8 - \frac{4}{\sqrt{1 + \left(\frac{L/2 + z_f}{R}\right)^2}} - \frac{4}{\sqrt{1 + \left(\frac{L/2 - z_f}{R}\right)^2}}. \quad (7)$$

This implies that for an extremely large-scale LIS, when  $L \gg R$ , or when  $R$  is fixed and  $L$  approaches infinity, the position along the  $z$ -axis consistently yields a fixed value of 8. Similarly,  $E_y$  on the central axis will also equal 8. However,  $E_z$ , due to significant differences in its expression, results in a different formula given as [17]

$$E_z(z_f) = \int_{-L/2}^{L/2} \int_0^{2\pi} \frac{R^2}{[R^2 + (l - z_f)^2]^{3/2}} d\theta dl = \frac{2\pi}{\sqrt{\left(\frac{R}{L/2 - z_f}\right)^2 + 1}} + \frac{2\pi}{\sqrt{\left(\frac{R}{L/2 + z_f}\right)^2 + 1}}. \quad (8)$$

Fig. 4.  $E_x$  vs  $x_f$ .

The value of  $E_z$  converges to  $4\pi$  as the length of the circular array approaches infinity. Fig. 3 shows the proportional relationship between  $E_x$  and  $E_z$  varies with different lengths. This also indicates that in an LIS system composed of vertically polarized transmitting arrays, the ratio of vertical polarization to horizontal polarization consistently remains constant at  $\pi/2$ . This suggests that near-field cross-polarization is independent of distance. Due to the asymmetry of  $E_x$  in the  $x$ - and  $y$ -directions, the transverse electric field distribution can be divided into two cases, with the focal points located at  $(x_f, 0, 0)$  and  $(0, y_f, 0)$ , respectively. However, due to the symmetry of  $E_z$ , only the case where the focal point is located at  $(x_f, 0, 0)$  needs to be considered. By solving under the closed approximation, the gain variation trend of  $E_x$  can be approximately obtained as following [17]:

$$E_x(x_f) \approx \begin{cases} \frac{4R}{k} [(k-1)K(u) + (1+k)E(u)], & 1 \leq k \\ 8, & 0 \leq k < 1 \end{cases} \quad (9)$$

where  $k = \frac{x_f}{R}$ ,  $u = \frac{4k}{(1+k)^2}$ . Here,  $K$  is the first kind of elliptic integral, and  $E$  is the second kind of elliptic integral. The numerical and analytical solutions are shown in Fig. 4. The 0 on the abscissa represents the starting point from the center of the circle. When  $L \gg R$ , the trends of the analytical solution and the numerical solution show a high degree of consistency. The electric field will converge to an exact numerical solution of 12500 V/m. Interestingly, the entire electric field distribution resembles a bathtub. Inside the circular array, the focal electric field is the same, while there are power peak regions outside. Similarly, by applying the same method, the simplified expression for  $E_x$  along the  $y$  can be obtained as [17]

$$E_x(y_f) = \frac{2}{y_f} \left( 2R + 2y_f - 2|R - y_f| + \sqrt{L^2 + 4(y_f - R)^2} - \sqrt{L^2 + 4(y_f + R)^2} \right). \quad (10)$$

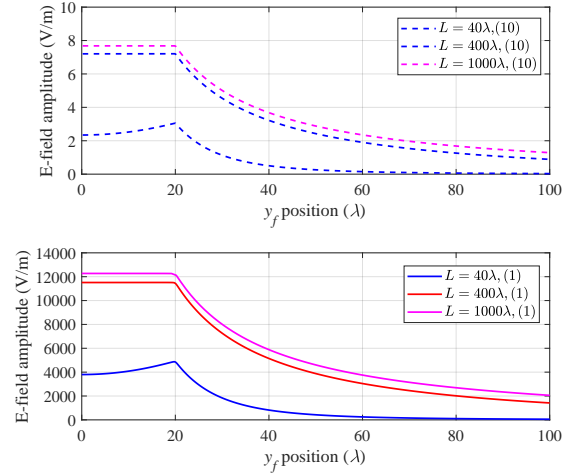
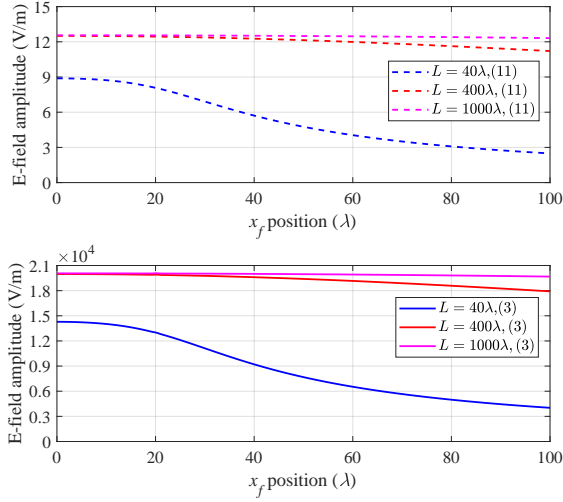
Fig. 5.  $E_x$  vs  $y_f$ .

Figure 5 presents the relationship between the position of the focal point along the  $y$ -axis and the electric field strength. The trends between analytical solution and the numerical solution exhibit a high degree of consistency for arrays of any length. Moreover, when the array size is long enough, the peak focused electric field strength along the  $y$ -axis converges to the same result as that along the  $x$ -axis. From the results of (9) and (10), it can be inferred that inside the array, during beam focusing,  $E_x$  and  $E_y$  always exhibit nearly identical intensity. The trend of the gain outside the cylinder is different from that of the focused electric field along the  $x$ -axis. The gain decreases as the electric field decreases. Considering the results of in these two different directions, in fact, when the length of the array reaches a certain size, which corresponds to the situation when the length of a certain corridor or room reaches a certain length in practice, the peak focused electric field in the space is approximately uniformly distributed. This means that we can reduce the number of components used to achieve the target power. It implies that when a user moves within the enclosed space inside the array, assuming the focal point automatically tracks the user's position, the user will always receive uniform charging or SNR. No adjustments are required on the user's end. The trend of the  $E_z$  along the  $x$ -axis can be simplified as [17]

$$E_z(x_f) = \frac{4K\left(\frac{-16Rx_f}{L^2+4(x_f-R)^2}\right)L}{\sqrt{L^2+4(x_f-R)^2}} + \frac{4K\left(\frac{16Rx_f}{L^2+4(x_f+R)^2}\right)L}{\sqrt{L^2+4(x_f+R)^2}}. \quad (11)$$

Figure 6 presents a comparison of equations (3) and (11) with their analytical solutions. The approximate peak electric field strength inside the cylinder is 20000 V/m. Unlike  $E_x$ , even with a relatively short array length (As set in the simulation, the radius is  $20\lambda$  and the array length is  $20\lambda$  (the actual physical size is 1 m)), the  $E_z$  can converge rapidly inside the cylinder to reach a uniformly focused level. This implies that  $E_z$  is more easily applicable in practice and has a lower requirement for the number of antenna elements.

Fig. 6.  $E_z$  vs  $x_f$ .

### B. Beamforming Resolutions

Next, we analyze the beam characteristics under different electric fields, mainly including the 3-dB beam width and the 3-dB beam depth. The focal point of  $E_z$  on the  $z$ -axis has its normalized gain varying along the  $z$ -axis direction (corresponding to focal depth) and the  $x$ -axis direction (corresponding to focal width) following the formulas below [17]:

$$E_z(\delta_d) \approx \begin{cases} 2\pi \left| \frac{e^{-j2\delta k \sin(\cos^{-1}(R/\sqrt{(L/2)^2 + R^2}))} - 1}{\delta k} \right|, & \delta \neq 0, \\ 4\pi, & \delta = 0. \end{cases} \quad (12)$$

$$E_z(\delta_w) \approx 4\pi |\text{sinc}(\delta_w k)|, \quad (13)$$

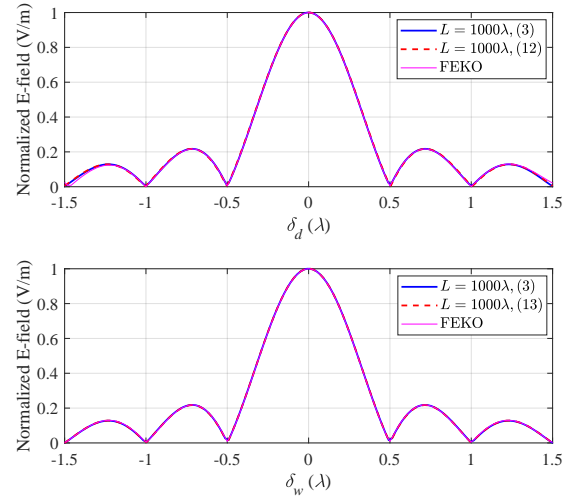
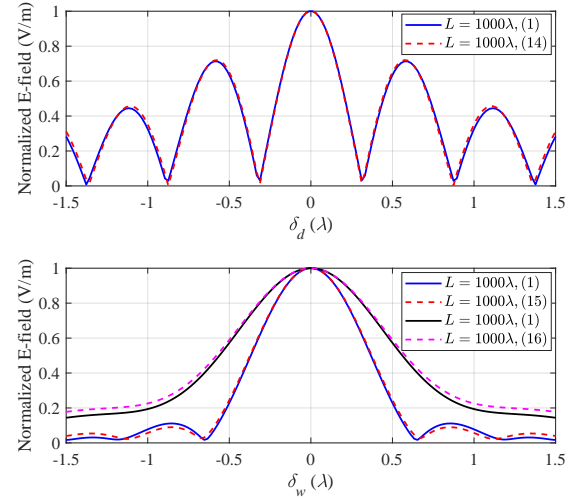
$$E_x(\delta_d) \approx 2\pi |H_{-1}(\delta_d k)|, \quad (14)$$

$$E_{xx}(\delta_w) \approx \begin{cases} \frac{2\pi H_0(\delta_w k)}{\delta_w k}, & \delta_w \neq 0, \\ 8, & \delta_w = 0. \end{cases} \quad (15)$$

$$E_{xy}(\delta_w) \approx \begin{cases} \frac{4Si(k\delta_w)}{k\delta_w}, & \delta_w \neq 0, \\ 8, & \delta_w = 0. \end{cases} \quad (16)$$

where  $H_{-1}$ ,  $H_0$  and  $Si$  are the -1-order, 0-order Struve function and the integral function of sine. As shown in Fig. 7 and 8, the numerical solution matches the analytical solution very well. Fig. 7 also presents the results obtained 2024 Altair FEKO software, which employed 200 rings with a radius of 0.1 mm. A high level of consistency was observed in the results. The 3-dB beamwidth and the beam depth of the  $E_z$  focal point at the focus are nearly equal, both being  $0.44\lambda$ , which indicates that the focal shape appears circular.

The focal point of  $E_x$  on the  $z$ -axis has its normalized gain varying along the  $z$ -axis direction (corresponding to focal depth) and along the  $x$ - and  $y$ -axis directions (corresponding

Fig. 7. Beam depth and beam width for  $E_z$ .Fig. 8. Beam depth and beam width for  $E_x$ .

to focal width) following the formulas below. Unlike the trend observed in  $E_z$ ,  $E_x$  exhibits more high-level sidelobes along the  $z$ -axis direction, meaning that multiple focal regions appear along the focal depth. The beamwidth of the main lobe is  $0.31\lambda$ , while along the  $x$ - and  $y$ -axis directions, the beam expands with beamwidths of  $0.54\lambda$  and  $0.84\lambda$ , respectively.

### III. CONCLUSIONS

This letter proposes some important properties in the near field for cylindrical dipole arrays. Three typical cases are studied when the focal points are at  $(x_f, 0, 0)$ ,  $(0, y_f, 0)$ , and  $(0, 0, z_f)$ . When the focal point is positioned along  $(0, 0, z_f)$ , apart from the region on both sides, the  $E_z$  and  $E_x$  approach normalized constant values of  $4\pi$  and  $8$ , respectively. The ratio between them remains approximately  $\pi/2$ . These insights can guide the development of regions capable of supporting future 6G mobile communications or power transmission.

## REFERENCES

- [1] S. Hu, F. Rusek, and O. Edfors, "Beyond massive MIMO: The potential of data transmission with large intelligent surfaces," *IEEE Trans. Signal Process.*, vol. 66, no. 10, pp. 2746-2758, May 2018.
- [2] C. H. Schmidt, M. M. Leibfritz and T. F. Eibert, "Fully probe-corrected near-field far-field transformation employing plane wave expansion and diagonal translation operators," *IEEE Trans. Antennas Propag.*, vol. 56, no. 3, pp. 737-746, March 2008.
- [3] S. Bosma, A. Neto, and N. Llombart, "On the near-field spherical wave formation in resonant leaky-wave antennas: application to small lens design," *IEEE Trans. Antennas Propag.*, vol. 70, no. 2, pp. 801-812, Feb. 2022.
- [4] R. Cornelius and D. Heberling, "Spherical wave expansion with arbitrary origin for near-field antenna measurements," *IEEE Trans. Antennas Propag.*, vol. 65, no. 8, pp. 4385-4388, Aug. 2017.
- [5] J. Garnica, R. A. Chinga and J. Lin, "Wireless power transmission: from far-field to near field," *Proceedings of the IEEE.*, vol. 101, no. 6, pp. 1321-1331, June 2013.
- [6] J. Li, Y. Zhu, Y. Hu, and W. Hong, "A miniaturized dual-polarized active phased array antenna for 5G millimeter-wave applications," *IEEE Antennas Wirel. Propag. Lett.* vol. 23, no. 2, pp. 618-622, Feb. 2024.
- [7] T. Arshed, S. Maci and E. Martini, "Direct synthesis of metasurfaces for efficient space- to surface-wave conversion and beamforming," *IEEE Trans. Antennas Propag.*, vol. 72, no. 10, pp. 7793-7806, Oct. 2024.
- [8] P. Nepa and A. Buffi, "Near-field-focused microwave antennas: near-field shaping and implementation," *IEEE Antennas Propag. Mag.*, vol. 59, no. 3, pp. 42-53, June 2017.
- [9] A. Buffi, P. Nepa, and G. Manara, "Design criteria for near-field-focused planar arrays," *IEEE Antennas Propag. Mag.*, vol. 54, no. 1, pp. 40-50, Feb. 2012.
- [10] A. Kosasih and E. Björnson, "Finite Beam Depth Analysis for Large Arrays," *IEEE Trans. Wireless Commun.*, vol. 23, no. 8, pp. 10015-10029, Aug. 2024.
- [11] V. Manohar and Y. Rahmat-Samii, "On the Resolution of Near-Field Focused Arrays," *IEEE Trans. Antennas Propag.*, Early Access, Nov, 2024.
- [12] G. Li, C. You, G. Shang and S. Wu, "Near-Field Communications With Extremely Large-Scale Uniform Arc Arrays: Channel Modelling and Performance Analysis," *IEEE Wireless Commun. Lett.*, Early Access, Jan, 2025.
- [13] J. W. Wu, R. Y. Wu, X. C. Bo, L. Bao, X. J. Fu and T. J. Cui, "Synthesis Algorithm for Near-Field Power Pattern Control and Its Experimental Verification via Metasurfaces," *IEEE Trans. Antennas Propag.*, vol. 67, no. 2, pp. 1073-1083, Feb. 2019.
- [14] Z. X. Huang and Y. J. Cheng, "Synthesis of Sparse Near-Field Focusing Antenna Arrays With Accurate Control of Focal Distance by Reweighted  $l_1$  Norm Optimization," *IEEE Trans. Antennas Propag.*, vol. 69, no. 5, pp. 3010-3014, May 2021.
- [15] Z. X. Huang, Y. J. Cheng and H. N. Yang, "Near-Field Pattern Synthesis for Sparse Focusing Antenna Arrays Based on Bayesian Compressive Sensing and Convex Optimization," *IEEE Trans. Antennas Propag.*, vol. 66, no. 10, pp. 5249-5257, Oct. 2018.
- [16] W. Chen, Z. Niu, Y. Ruan, Y. Ding and C. Gu, "Structured Sparsity Learning with Group  $L_{1/2}$  Regularization for Efficient Synthesis of Near-Field Multi-Focus Sparse Planar Arrays," *IEEE Antennas Wireless Propag. Lett.*, Early Access, Feb, 2025.
- [17] A. Jeffrey, H. Dai, *Handbook of Mathematical Formulas and Integrals*, 4th Ed., Elsevier, Jan, 2008.